



Title	Identification of the infrasound signals emitted by explosive eruption of Mt. Shinmoedake by three-dimensional ray tracing
Author(s)	Saito, Hiroaki; Yamamoto, Tetsuo; Nakajima, Kensuke; Kuramoto, Kiyoshi; Yamamoto, Masa-yuki
Citation	Journal of the acoustical society of America, 149(1), 591-598 https://doi.org/10.1121/10.0003366
Issue Date	2021-01
Doc URL	http://hdl.handle.net/2115/83892
Rights	This article may be downloaded for personal use only. Any other use requires prior permission of the author and AIP Publishing. This article appeared in The Journal of the Acoustical Society of America 149, 591-598 (2021) and may be found at https://doi.org/10.1121/10.0003366 .
Type	article
File Information	J. Acoust. Soc. Am.149-1_591-598.pdf



[Instructions for use](#)

Identification of the infrasound signals emitted by explosive eruption of Mt. Shinmoedake by three-dimensional ray tracing

Hiroaki Saito, Tetsuo Yamamoto, Kensuke Nakajima, Kiyoshi Kuramoto, and Masa-yuki Yamamoto

Citation: *The Journal of the Acoustical Society of America* **149**, 591 (2021); doi: 10.1121/10.0003366

View online: <https://doi.org/10.1121/10.0003366>

View Table of Contents: <https://asa.scitation.org/toc/jas/149/1>

Published by the [Acoustical Society of America](#)

ARTICLES YOU MAY BE INTERESTED IN

[Probability of detection of electric vehicles with and without added warning sounds](#)

The Journal of the Acoustical Society of America **149**, 599 (2021); <https://doi.org/10.1121/10.0003386>

[Feit's seminal article on radiation of sound by a vibrating plate](#)

The Journal of the Acoustical Society of America **149**, R1 (2021); <https://doi.org/10.1121/10.0002422>

[Improved multimodal formulation of the wave propagation in a 3D waveguide with varying cross-section and curvature](#)

The Journal of the Acoustical Society of America **149**, 476 (2021); <https://doi.org/10.1121/10.0003336>

[The spectrogram, method of reassignment, and frequency-domain beamforming](#)

The Journal of the Acoustical Society of America **149**, 747 (2021); <https://doi.org/10.1121/10.0003384>

[An arbitrary high-order discontinuous Galerkin method with local time-stepping for linear acoustic wave propagation](#)

The Journal of the Acoustical Society of America **149**, 569 (2021); <https://doi.org/10.1121/10.0003340>

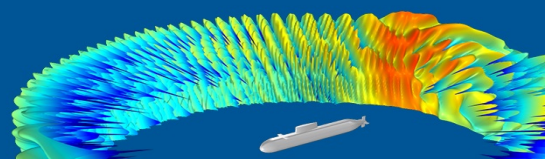
[Highlighting interlanguage phoneme differences based on similarity matrices and convolutional neural network](#)

The Journal of the Acoustical Society of America **149**, 508 (2021); <https://doi.org/10.1121/10.0003339>

COMSOL Day
Acoustics

A free, online event where you can attend multiphysics simulation sessions, ask COMSOL staff your questions, and more

JOIN US MAY 25 >>



Identification of the infrasound signals emitted by explosive eruption of Mt. Shinmoedake by three-dimensional ray tracing

Hiroaki Saito,^{1,a)} Tetsuo Yamamoto,^{2,b)} Kensuke Nakajima,^{3,c)} Kiyoshi Kuramoto,^{1,d)} and Masa-yuki Yamamoto^{4,e)}

¹Department of CosmoSciences, Hokkaido University, Sapporo, Hokkaido 060-0810, Japan

²Institute of Low Temperature Science, Hokkaido University, Sapporo, Hokkaido 060-0819, Japan

³Department of Earth and Planetary Sciences, Faculty of Sciences, Kyushu University, Fukuoka, Fukuoka 819-0395, Japan

⁴School of Systems Engineering, Kochi University of Technology, Kami, Kochi 782-8502, Japan

ABSTRACT:

Mt. Shinmoedake, a part of the Mt. Kirishima cluster of volcanoes in Kyushu, Japan, erupted on 10 March 2018. Our infrasound sensor network located at a distance of more than 200 km from the source detected signals emitted by an explosive eruption of Mt. Shinmoedake. The arrival time of the signals is divided into three time intervals. To reveal how the observed infrasound signals propagated from the source to the sensors, we carry out three-dimensional ray tracing on the basis of the Hamilton equations including the vertical profiles of the temperature and wind around the ray path. We present formulas for calculating travel time and distance of infrasound from a source to an observation site and its turning altitude in the atmosphere. We have identified four kinds of signals, namely, the waves propagated in the troposphere undergoing multiple refraction and those refracting from the stratosphere, the mesosphere, and the lower thermosphere. Brief discussion is devoted to some of the unidentified signals.

© 2021 Acoustical Society of America. <https://doi.org/10.1121/10.0003366>

(Received 29 September 2020; revised 30 December 2020; accepted 31 December 2020; published online 25 January 2021)

[Editor: Steffen Marburg]

Pages: 591–598

I. INTRODUCTION

Infrasound is inaudible sound of frequencies lower than 20 Hz and can propagate for a long distance with little attenuation. This characteristic is suitable for the detection of distant huge events such as tsunamis, typhoons, tornados, volcanic eruptions, and nuclear tests [e.g., Bedard and Georges (2000), Campus (2004), and Headlin *et al.* (2002)]. The Comprehensive Nuclear-Test-Ban Treaty Organization (CTBTO) has been establishing the International Monitoring System (IMS) consisting of 60 sites of infrasound sensors around the world (Christie and Campus, 2010) to estimate the source position and the scale of geo-hazards as well as nuclear tests.

It is predicted that Japan is threatened by a Nankai Trough earthquake of M8–M9 within 30 years (Headquarters for Earthquake Research Promotion, 2013) with a probability of $\sim 70\%$. In the course of this earthquake, it is also predicted that a tsunami with a height of more than 10 m will hit a large area along the Pacific Coast longer than 1000 km in the southwest region of Japan. For the mitigation of the tsunami disaster, we have developed an infrasound sensor, ADXII-INF01, in cooperation with SAYA Inc., and we have constructed a dense network of infrasound sensors

in Kochi, Japan (Yamamoto and Yokota, 2015). The ADXII-INF01 covers the frequencies of 10^{-3} to 6.25 Hz with a data polling rate of 4 Hz. The sensor network located more than 200 km away from Mt. Shinmoedake detected infrasound signals emitted by its explosive eruption on 10 March 2018. To clarify the nature of the observed wave signals, we have done an analysis of the observed signals by ray tracing calculations, and we have identified waves refracted from the troposphere, the stratosphere, the mesosphere, and the thermosphere.

In Sec. II, we show the observational data obtained from the explosive eruption of Mt. Shinmoedake. Section III describes a ray tracing formulation based on the Hamilton equations; we present equations for calculating the ray paths and formulas for travel time and travel distance of infrasound to the observation sites. In Sec. IV, we compare the results of the ray tracing calculations with the observed travel time and distance of the infrasound and identify the nature of the observed signals. Summary and discussion are given in Sec. V.

II. INFRASOUND OBSERVATIONS OF EXPLOSIVE ERUPTIONS OF MT. SHINMOEDAKE

Mt. Shinmoedake is a part of the Mt. Kirishima cluster of volcanoes on Kyushu Island, Japan. The volcano is located at 31.91° N, 130.88° E, and its elevation is 1412 m. It is recorded to have erupted in the years 1716, 1717, 1822, 1959, 1991, 2008, 2009, 2011, 2017, and 2018. A recent explosive eruption associated with atmospheric pressure

^{a)}Electronic mail: saito.hiroaki@me.com, ORCID: 0000-0001-7937-2971.

^{b)}ORCID: 0000-0001-6071-330X.

^{c)}ORCID: 0000-0002-0333-2364.

^{d)}ORCID: 0000-0002-6757-8064.

^{e)}ORCID: 0000-0003-3191-6970.

pulses and a seismic tremor was observed on 6 March 2018. The explosive eruptions occurred that year more than 40 times in March and once in April and June, respectively.

During the explosive eruptions in March, atmospheric pressure pulses stronger than 100 Pa were observed several times by the microbarometer MB2005 installed by the Earthquake Research Institute (ERI), University of Tokyo. At the time of eruption, the microbarometer was located 3 km away from the crater of Mt. Shinmoedake and was located at 31.89° N, 130.86° E. The microbarometer covered a frequency range of 0.01–4 Hz, and its sampling rate was 100 Hz. The eruption of Mt. Shinmoedake observed at 1:54 (Japan Standard Time, JST) on 10 March 2018 produced the most significant atmospheric pressure pulses in the eruptions that occurred in 2018. Figure 1 shows atmospheric pressure pulses received by the sensor of ERI, indicating that the observed highest pressure was 610 Pa at 01:54:43 (JST) (Ichihara, 2018).

Our infrasound sensor network located more than 200 km away from Mt. Shinmoedake also detected and recorded the signals. Figure 2 shows the locations of our infrasound sensors on Shikoku Island, Japan. They are located in the region of $204 < r < 343$ km from Mt. Shinmoedake and $25^\circ < \varphi < 37^\circ$, where φ is the azimuth angle of the sensors measured counterclockwise from eastward, taking the origin at Mt. Shinmoedake. Table I summarizes the distance r of the sensor sites measured from Mt. Shinmoedake and their azimuth angle φ .

Figure 3 shows bandpass-filtered waveforms received by the sensors at the polling rate of 4 Hz at sites 1–6 in the frequency range of 0.05–0.3 Hz, which implies a spatial resolution of 6 km for each of the sites. The highest atmospheric pressure pulse detected by each of the sensors was between 1.0 and 1.5 Pa.

Table I summarizes the standard deviation σ for all sites. The standard deviation of the ambient sound pressure at each site was calculated on the basis of the observed data for 24 h on 10 March 2018. We regard the observed sound pressure higher than the 3.0σ level to be the signals. To clarify the wavepackets in Fig. 3, we assume the signals detected intermittently whose time interval is shorter than 10 s to be one group; the time interval corresponds to a frequency of 0.1 Hz. At least two wavepackets are identified in

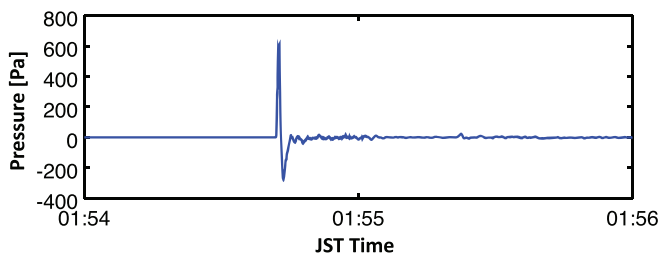


FIG. 1. (Color online) Time evolution of the atmospheric pressure pulses observed at the explosive eruption on 10 March 2018 by the MB2005 sensor located at 3 km from Mt. Shinmoedake. The peak pressure was 610 Pa at 01:54:43 (JST) (Ichihara, 2018).

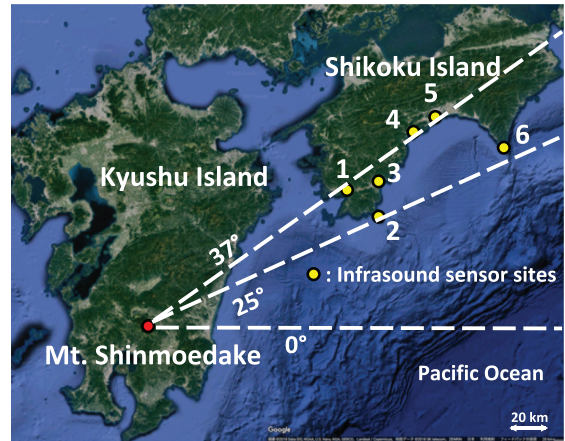


FIG. 2. (Color online) Locations of Mt. Shinmoedake (red filled circle) and our infrasound sensors (yellow filled circles) on Shikoku Island. The sensors are located in the area of the azimuth angle of $25^\circ < \varphi < 37^\circ$.

Fig. 3. Furthermore, we identify the signals of the 3σ -confidence level at sites 1–6 in time interval 3 as indicated by red arrows in Fig. 3. The durations of time intervals 1–3 at sites 1–6 are summarized in Table II. We shall examine these features in Sec. IV by the ray tracing of the infrasound emitted from Mt. Shinmoedake.

III. ACOUSTIC WAVE PROPAGATION IN A STRATIFIED ATMOSPHERE

In the present observation, the propagation distance of the wave to the sites (200–340 km) is much longer than the wavelength (< 6 km). In such a situation, one can introduce the concept of a ray in discussing its propagation and can apply geometrical acoustics [e.g., Landau and Lifshitz (1959)], in which the wave is propagated along a ray whose tangent is parallel to the wavevector at any point.

The formulation discussed here follows that presented by Landau and Lifshitz (1959) and is analogous to calculating the motion of a particle using Hamilton equations [see also Blom (2019), Jones and Bedard (2018), and Lighthill (1978)]. Analogous Hamilton equations for a wave of angular frequency ω and wavevector \mathbf{k} are given by

$$\dot{\mathbf{r}} = \left(\frac{\partial \omega}{\partial \mathbf{k}} \right)_{\mathbf{r}}, \quad \dot{\mathbf{k}} = - \left(\frac{\partial \omega}{\partial \mathbf{r}} \right)_{\mathbf{k}}, \quad (1)$$

TABLE I. Distances r of the sensor sites from the source, azimuth angles φ and standard deviations σ of the atmospheric pressure pulses observed for 24 h on 10 March 2018 at sites 1–6.

	Name	r (km)	φ (deg)	σ (Pa)
Site 1	Sukumo	204.8	33	3.3×10^{-2}
Site 2	Tosashimizu	219.4	25	1.3×10^{-1}
Site 3	Kuroshio	239.5	32	8.7×10^{-2}
Site 4	Tosa	295.2	36	6.1×10^{-2}
Site 5	Kochi	303.2	37	5.2×10^{-2}
Site 6	Muroto	342.7	27	8.4×10^{-2}

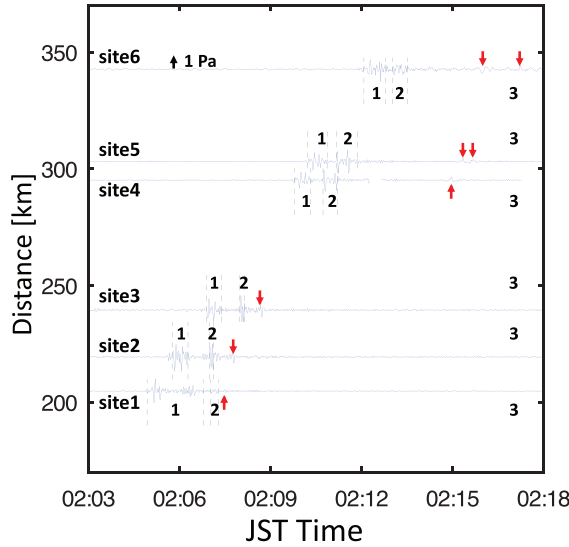


FIG. 3. (Color online) Bandpass-filtered waveforms observed at sites 1–6 after the eruption at 01:54 JST on 10 March 2018. Time intervals of the two signal packets are indicated by the vertical dashed lines (see the text for details). Red arrows indicate the signals obtained in time interval 3.

where \mathbf{r} denotes the position vector. Note that ω corresponds to Hamiltonian and \mathbf{k} to momentum in particle mechanics. The first equation gives the group velocity of propagation of the wave, and the second one determines the time variation of the wavevector. If the atmospheric conditions can be regarded to be in the steady state ($\partial\omega/\partial t = 0$) during wave propagation, we see from Eq. (1) that ω is kept constant along a ray path, since

$$\frac{d\omega}{dt} = \frac{\partial\omega}{\partial t} + \dot{\mathbf{r}} \cdot \frac{\partial\omega}{\partial \mathbf{r}} + \dot{\mathbf{k}} \cdot \frac{\partial\omega}{\partial \mathbf{k}} = 0. \quad (2)$$

Considering acoustic wave propagation for no wind in the atmosphere, one has the dispersion relation given by

$$\omega = ck, \quad (3)$$

where c is sound speed and $k = |\mathbf{k}|$. A wave is expressed by

$$\psi = \text{const} \cdot \exp[i(\mathbf{k} \cdot \mathbf{r} - ckt)] \quad (4)$$

with the use of the dispersion relation given by Eq. (3), where i is the imaginary unit. This dispersion relation is applicable under the condition that the effect of gravity and

the Earth’s rotation can be ignored [e.g., Scott *et al.* (2017)]. Namely, it holds for frequencies of $\omega/2\pi \gg g/2\pi c \sim 5 \times 10^{-3} \text{ Hz} \gg \Omega/\pi \sim 2.3 \times 10^{-5} \text{ Hz}$, where $g = 9.8 \text{ m/s}^2$ is the standard acceleration of gravity and $\Omega = 7.3 \times 10^{-5} \text{ rad/s}$ is the angular speed of Earth’s rotation [see Jones and Bedard (2018)].

Equation (3) is a dispersion relation for no wind in the atmosphere. The dispersion relation in the presence of wind is derived in the following manner. Let \mathbf{K} be a wind-blowing inertial system and \mathbf{K}' be another inertial system moving with wind velocity \mathbf{u} relative to \mathbf{K} . The position vector \mathbf{r}' and the wavevector \mathbf{k}' in \mathbf{K}' are given (Landau and Lifshitz, 1959) by

$$\mathbf{r}' = \mathbf{r} - \mathbf{u}t, \quad \mathbf{k}' = \mathbf{k}. \quad (5)$$

There is no wind in \mathbf{K}' ; thus, the wave observed in \mathbf{K}' is given by $\psi \propto \exp[i(\mathbf{k}' \cdot \mathbf{r}' - ck't)]$, where c is sound speed in the system with no wind. In consequence, the wave expressed in terms of the quantities in \mathbf{K} is expressed by

$$\psi = \text{const} \cdot \exp\{i[\mathbf{k} \cdot \mathbf{r} - (ck + \mathbf{u} \cdot \mathbf{k})t]\}, \quad (6)$$

indicating that the dispersion relation in the wind-blowing system \mathbf{K} is given by

$$\omega = ck + \mathbf{u} \cdot \mathbf{k}. \quad (7)$$

Let us examine the situation in which the wind velocity \mathbf{u} is horizontal and varies with altitude z in the region of concern. We assume that \mathbf{u} is uniform in the horizontal plane at each altitude z . Namely, the wind velocity field is written as $\mathbf{u} = (u_x(z), u_y(z), 0)$, where we assume that \mathbf{u} is steady during the propagation of the wave. The dispersion relation (7) is then expressed by

$$\omega = ck + u_x k_x + u_y k_y, \quad (8)$$

and the results of the Hamilton equations (1) are given by

$$\dot{x} = c \frac{k_x}{k} + u_x, \quad (9)$$

$$\dot{y} = c \frac{k_y}{k} + u_y, \quad (10)$$

$$\dot{z} = c \frac{k_z}{k}, \quad (11)$$

$$\dot{k}_x = \dot{k}_y = 0, \quad (12)$$

$$\dot{k}_z = -k \frac{dc}{dz} - k_x \frac{du_x}{dz} - k_y \frac{du_y}{dz}. \quad (13)$$

Equation (12) indicates that the wavevector projected onto the xy -plane is constant in time.

We express constant k_x and k_y in terms of the spherical coordinates as

$$k_x = k_0 \sin \theta_0 \cos \phi_0, \quad k_y = k_0 \sin \theta_0 \sin \phi_0, \quad (14)$$

TABLE II. Duration of the time intervals (TIs) 1, 2, and 3 at sites 1–6.

Sensor	TI 1 (s)	TI 2 (s)	TI 3 (s)
Site 1	624–735	750–766	>766
Site 2	675–705	747–755	>755
Site 3	742–771	807–817	>817
Site 4	916–948	972–1001	>1001
Site 5	941–980	998–1040	>1040
Site 6	1053–1096	1110–1139	>1139

where k_0 is the wavenumber at $t=0$, and θ_0 and ϕ_0 are the initial zenith and azimuth angles, respectively. The dispersion relation (8) is then expressed by

$$\omega = c(z)k(z) + U(z; \phi_0)k_0 \sin \theta_0, \quad (15)$$

where

$$U(z; \phi_0) = u_x(z) \cos \phi_0 + u_y(z) \sin \phi_0 = \mathbf{u} \cdot \hat{\mathbf{h}}_0 \quad (16)$$

with

$$\hat{\mathbf{h}}_0 = (\cos \phi_0, \sin \phi_0, 0) \quad (17)$$

being a horizontal unit vector parallel to \mathbf{k}_0 projected onto the xy -plane. Note that U is independent of θ_0 .

If \dot{z} turns to be $\dot{z} < 0$ at a certain altitude, the wave emitted upward from $z=0$ in the direction (θ_0, ϕ_0) turns its path downward at this altitude. The turning altitude z_t is characterized by $\dot{z} = 0$, namely, $k_z(z_t) = 0$ from Eq. (11), in consequence $k(z_t) = k_0 \sin \theta_0$. Equating ω given by Eq. (15) at $z = z_t$ and the source altitude z_0 in view of the invariance of ω along a ray path [see Eq. (2)], one obtains the equation that determines the turning altitude z_t , namely,

$$[c(z_t) + U(z_t; \phi_0) - U(z_0; \phi_0)] \sin \theta_0 = c(z_0). \quad (18)$$

The wavenumber k at altitude z is calculated by equating ω given by Eq. (15) at the altitudes of z and z_t . The result is given by

$$k = \frac{k_0 \sin \theta_0}{c} [c(z_t) + U(z_t; \phi_0) - U(z, \phi_0)]. \quad (19)$$

Since $k = \sqrt{k_z^2 + k_x^2 + k_y^2} = \sqrt{k_z^2 + k_0^2 \sin^2 \theta_0}$, Eq. (19) leads to

$$k_z = \pm \frac{k_0 \sin \theta_0}{c} \sqrt{[c(z_t) + U(z_t; \phi_0) - U(z; \phi_0)]^2 - c^2}. \quad (20)$$

The time required to reach the turning altitude z_t is calculated with the use of Eq. (11), which yields

$$dt = \frac{k}{ck_z} dz. \quad (21)$$

Substituting k given by Eq. (19) and k_z given by Eq. (20) expressed as functions of z into Eq. (21), we obtain

$$dt = \pm \frac{dz}{c} \frac{c(z_t) + U(z_t; \phi_0) - U(z; \phi_0)}{\sqrt{[c(z_t) + U(z_t; \phi_0) - U(z; \phi_0)]^2 - c^2}}, \quad (22)$$

where the plus and minus signs should be adopted for the upward ($dz > 0$) and downward ($dz < 0$) propagation of the wave, respectively. The following equations [Eqs. (23) and (25)–(28)] are those for upward propagation. From the time reversal symmetry, the travel time from $z = z_0$ to $z = z_t$ is equal to that from $z = z_t$ to $z = z_0$. Expressing the time for

the wave to reach the turning altitude z_t from $z = z_0$ by $\tau/2$, we have

$$\frac{\tau}{2} = \int_{z_0}^{z_t} \frac{dz}{c} \frac{c(z_t) + U(z_t; \phi_0) - U(z; \phi_0)}{\sqrt{[c(z_t) + U(z_t; \phi_0) - U(z; \phi_0)]^2 - c^2}}. \quad (23)$$

The x -coordinate of the turning point is calculated from Eqs. (9) and (11), which yield

$$\frac{dx}{dz} = \frac{ck_0 \sin \theta_0 \cos \phi_0 + u_x k}{ck_z} \quad (24)$$

with the use of Eq. (14). Substituting Eqs. (19) and (20) into Eq. (24), we obtain

$$dx = \frac{dz}{c} \frac{c^2 \cos \phi_0 + u_x [c(z_t) + U(z_t; \phi_0) - U(z, \phi_0)]}{\sqrt{[c(z_t) + U(z_t; \phi_0) - U(z, \phi_0)]^2 - c^2}}. \quad (25)$$

The x -coordinate $X/2$ of the turning point at $z = z_t$ of the wave starting from a source at the origin is given by

$$\frac{X}{2} = \int_{z_0}^{z_t} \frac{dz}{c} \frac{c^2 \cos \phi_0 + u_x [c(z_t) + U(z_t; \phi_0) - U(z, \phi_0)]}{\sqrt{[c(z_t) + U(z_t; \phi_0) - U(z, \phi_0)]^2 - c^2}}. \quad (26)$$

In a similar manner, the y -coordinate $Y/2$ is obtained to be

$$\frac{Y}{2} = \int_{z_0}^{z_t} \frac{dz}{c} \frac{c^2 \sin \phi_0 + u_y [c(z_t) + U(z_t; \phi_0) - U(z, \phi_0)]}{\sqrt{[c(z_t) + U(z_t; \phi_0) - U(z, \phi_0)]^2 - c^2}}. \quad (27)$$

The end point $\mathbf{R} = (X, Y, z_0)$ of a path of the ray emitted from the source $(0, 0, z_0)$ is expressed by

$$\frac{\mathbf{R}}{2} = \int_{z_0}^{z_t} \frac{dz}{c(z)} \frac{c(z)^2 \hat{\mathbf{h}}_0 + \mathbf{u}(z) \cdot [c(z_t) + (\mathbf{u}(z_t) - \mathbf{u}(z)) \cdot \hat{\mathbf{h}}_0]}{\sqrt{[c(z_t) + (\mathbf{u}(z_t) - \mathbf{u}(z)) \cdot \hat{\mathbf{h}}_0]^2 - c^2(z)}} \quad (28)$$

with the use of Eq. (17).

In the following, we set $z_0 = 0$ unless otherwise stated.

IV. IDENTIFICATION OF THE DETECTED SIGNALS

A. Temperature and wind speed profiles

We calculate ray paths and travel time for the infrasound emitted from the source at Mt. Shinmoedake. We employ the Mass Spectrometer and Incoherent Scatter Radar Extended model (NRLMSISE-00) (Picone *et al.*, 2002) for the vertical profile of the temperature. Figure 4(a) shows the vertical profile of the temperature T , and Fig. 4(b) shows sound speed c calculated by using the temperature profile. For the wind profiles, we use Horizontal Wind Model 2014 (HWM14) (Drob *et al.*, 2015) and Modern-Era

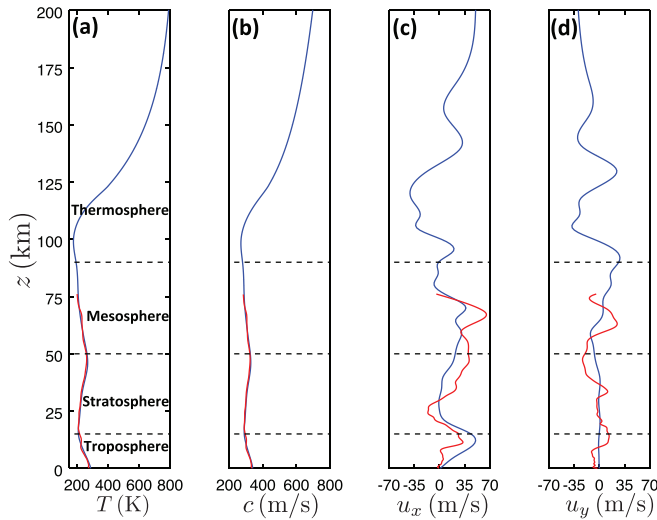


FIG. 4. (Color online) (a) Vertical profiles of the temperature T given by NRLMSISE-00 (blue) (Picone *et al.*, 2002) and MERRA-2 (red) (Gelaro *et al.*, 2017). (b) Sound speed c calculated with the use of the temperature profiles given by NRLMSISE-00 (blue) and MERRA-2 (red). (c) and (d) Vertical profiles of zonal (c) and meridional (d) wind velocities u_x and u_y given by HWM14 (Drob *et al.*, 2015) (blue) and MERRA-2 (red).

Retrospective analysis for Research and Applications, version 2 (MERRA-2) (Gelaro *et al.*, 2017). HWM14 is an empirical model based on the observations from the ground and satellites for 50 years and reproduces long-term averaged climatology of the atmosphere (Drob *et al.*, 2015). MERRA-2, developed by the Global Modeling Assimilation Office of NASA (Gelaro *et al.*, 2017), is an atmospheric reanalysis dataset based on satellite and ground-based observations. MERRA-2 provides reanalysis data with time resolution of 3 h and a spatial resolution of $0.5^\circ \times 0.625^\circ$ in longitude and latitude (Global Modeling and Assimilation Office (GMAO), 2015). Figures 4(c) and 4(d) show the vertical profiles of zonal (positive to the east) wind u_x and meridional (positive to the north) wind u_y . We interpolated u_x and u_y given by MERRA-2 at 0:00 and 3:00 JST to deduce those at 2:00 on 10 March 2018 in the area of Mt. Shinmoedake (31.9° N, 130.9° E). The HWM14 profile is shown in blue and the MERRA-2 profile in red for comparison.

In the following, we adopt HWM14 for the altitude of $z \leq 200$ km, which is set to include all rays falling onto all of the sites. For the rays confined in $z \leq 76$ km, we use MERRA-2.

B. Turning altitudes

Figure 5 shows examples of paths of the rays emitted toward the site 5 ($\phi_0 = 37^\circ$) for the initial zenith angles $\theta_0 = 30^\circ, 65^\circ,$ and 85° . Here, we used HWM14 for the wind profile and set $z_0 = 0$, since the turning altitudes are much higher than the source altitude as will be seen below. Figure 5(a) indicates the ray paths projected onto the xy -plane together with those for the windless case by a dashed line for reference. The deviation of the end points of the sound rays from the line connecting the source and site 5 less than 3° . The deviation angles for the other sites are

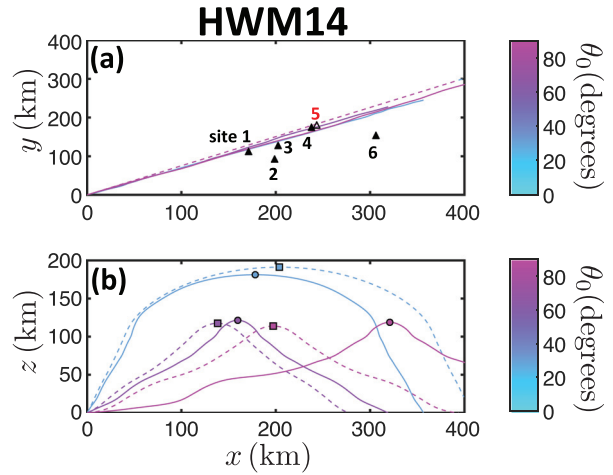


FIG. 5. (Color online) Sound ray paths projected onto the xy -plane (a) and the xz -plane (b) for the rays emitted toward the site 5 ($\phi_0 = 37^\circ$). The wind profiles used here are HWM14. The dashed lines indicate ray paths for the windless case. Initial zenith angle θ_0 is indicated by the color-code on the right-hand side. Triangles in (a) indicate the sensor sites. In (b), the turning altitudes of the rays are shown by the circles; those for the windless case are shown by the squares for comparison.

around 3° as well. Figure 5(b) shows paths of those rays projected onto the xz -plane, indicating that the rays return to the ground for $\theta_0 \geq 30^\circ$, for which the turning altitudes are $z_t \sim 110$ km.

The observed signals include the rays that turn at some altitudes. Turning altitude z_t for the sound emitted toward the direction (θ_0, ϕ_0) is given by the solution of Eq. (18), namely, the solution of the equation

$$f(z; \phi_0) = \frac{1}{\sin \theta_0}, \quad (29)$$

where

$$f(z; \phi_0) = \frac{c(z) + U(z; \phi_0) - U(z_0; \phi_0)}{c(z_0)}. \quad (30)$$

Figure 6 illustrates $f(z; \phi_0)$ toward site 5 ($\phi_0 = 37^\circ$). For a turn of a ray to occur, θ_0 must be larger than a certain value because $f(z; \phi_0)$ as a function of z is bounded at the altitudes z of interest, i.e., $0 < z < 200$ km. The turning altitude z_t of the sound emitted toward the initial azimuth angle ϕ_0 is given by the value of z at the intersection of the curve $f(z; \phi_0)$ and the vertical line at $1/\sin \theta_0$ in Fig. 6. If there are multiple solutions that satisfy Eq. (29), the lowest z_t gives the actual turning altitude within the framework of geometric acoustics. Figures 5, 6, and 8 indicate that there are four possible turning altitudes. They are in the lower thermosphere [$z_t > 110$ km; Figs. 5(b) and 6(a)], the mesosphere [$60 < z_t < 66$ km; Fig. 6(b)], the stratosphere [$42 < z_t < 45$ km; Fig. 6(b)], and the troposphere [$z_t \sim 10$ km; Figs. 6(b) and 8].

C. Signals in time interval 1

Figure 7 shows the relation of the travel time τ and horizontal range r of the rays that fall on the line $\phi = \phi_i$ ($i = 1, \dots, 6$).

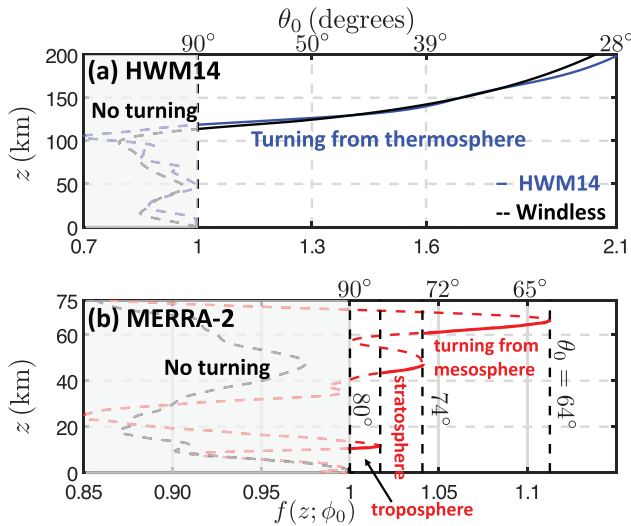


FIG. 6. (Color online) The function $f(z; \phi_0)$ defined by Eq. (30) for HWM14 (blue) and MERRA-2 (red) for the rays emitted toward site 5 ($\phi_0 = 37^\circ$). The windless cases are shown by the black dashed thin lines. The gray shaded areas in (a) and (b) indicate the regions of $f(z; \phi_0) < 1$. The upper horizontal axes of both panels indicate the initial zenith angle θ_0 .

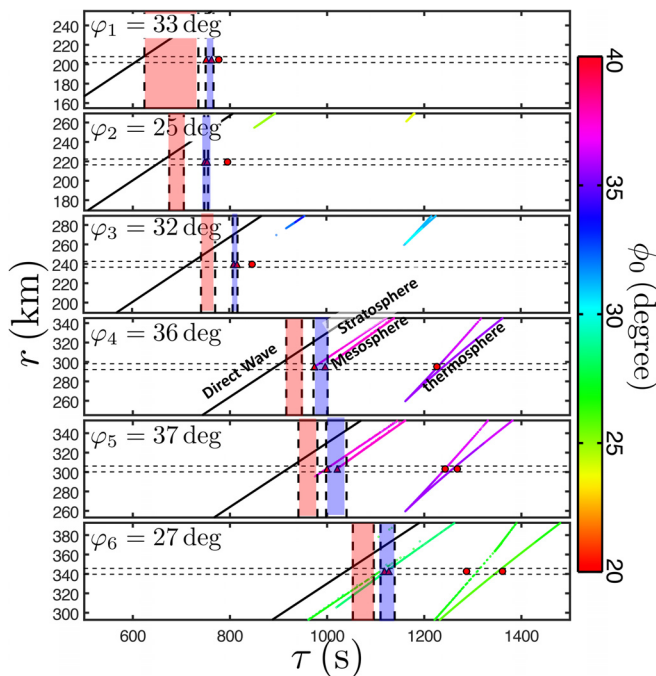


FIG. 7. (Color online) Travel time τ versus horizontal distance r for the rays falling onto the line $\phi = \phi_i$ ($i = 1, \dots, 6$), where ϕ_i is the azimuth angle of the i th site. The black lines indicate the τ - r relation for direct waves propagated horizontally at the sound speed of 334 m/s estimated from the surface temperature, and the lines of the other colors are those for the rays turning from the stratosphere, mesosphere, and thermosphere shown in the figure. Horizontal dashed lines in each panel indicate the distance $r_i \pm 3$ km from the source to the i th sensor. The semi-transparent red and blue shaded areas indicate time intervals 1 and 2, respectively. The color-code of ϕ_0 indicates azimuth angle ϕ_0 of the ray at the source. The red filled circles indicate the signals in time interval 3, and the red filled triangles indicate the first and second maxima of the signals in time interval 2.

The red and blue shaded areas indicate time intervals 1 and 2, respectively. Here, we define the “end point” of the ray by a circle of radius 3 km in view of the limitation on the spatial resolution of the wave of frequency ~ 0.05 Hz. The intervals of the initial azimuth and zenith angles are taken to be $25^\circ < \phi_0 < 40^\circ$ and $0^\circ < \theta_0 < 90^\circ$ with their increments of 0.1° in drawing the figure of τ versus r .

We can expect that the signals detected in time interval 1 are a direct wave propagated horizontally near the ground surface ($z_0 = 0$). Apparent sound speed estimated from the distance and observed travel time between the source and each of the sites is 317 m/s, which corresponds to a surface temperature of -25°C . On the other hand, the sound speed is calculated to be 334 m/s if we adopt the surface temperature of 3.5°C , which is the temperature averaged over five places near Mt. Shinmoedake and the observation sites (observation data by the Japan Meteorological Agency). This result suggests that the signals detected in time interval 1 are not simply sound waves propagated horizontally.

To reveal the reason why the observed speed of the wave is slower than the calculated one, we investigate the wave propagation in the troposphere in detail. In the propagation in the troposphere, the source altitude cannot be set to be $z_0 = 0$ km because the elevation of Mt. Shinmoedake cannot be ignored compared with the altitude of the tropopause. We carried out ray tracing calculations by varying the source altitude in $0 < z_0 < 6$ km. We found that the rays arrive at all sites and are propagated near the ground surface for the source at $z_0 = 2.5$ km. Figure 8(b) shows some of the paths of the rays emitted from the source at $z_0 = 2.5$ km toward the direction of the site 5 ($\phi_0 = 37^\circ$) for $\theta_0 = 75^\circ, 80^\circ, 86^\circ$, and 88° together with $c(z) + U(z; \phi_0)$ in Fig. 8(a). The rays emitted at $86^\circ < \theta_0 < 90^\circ$ are confined in $2 < z < 10$ km, those at $85^\circ < \theta_0 < 86^\circ$ are confined in $0 < z < 10$ km and near the ground surface, those at $78^\circ < \theta_0 < 85^\circ$ turn once at $z \sim 10$ km and fall to the ground surface, and those at $\theta_0 < 78^\circ$ do not turn at the troposphere. The figure indicates that the ray is not propagated straight horizontally but undergoes multiple refraction, which occurs because the z -component of the wavevector tends to be propagated downward at altitudes of $dc/dz > 0$ and $du_x/dz > 0$ and vice versa [see Eq. (13)]. In the present

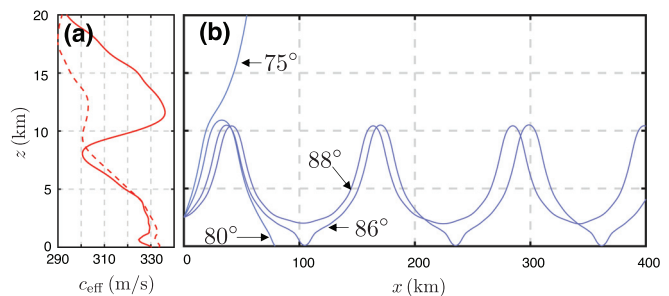


FIG. 8. (Color online) (a) Vertical profile of c (dashed line) and $c_{\text{eff}} \equiv c(z) + U(z; 37^\circ)$ (solid line) calculated by using MERRA-2, where $U(z; 37^\circ)$ is the wind speed toward the site 5 ($\phi_0 = 37^\circ$). (b) example of ray paths projected onto the xz -plane. The numbers attached to the curves are the initial zenith angles θ_0 .

case, the turns at the high altitude are mainly the result of the tropospheric jet stream around $z \sim 10$ km (see Fig. 8), and those at the low altitude are due to the negative temperature gradient ($dT/dz < 0$). Net horizontal propagation speeds deduced from the travel times are 316–320 m/s for sites 1–6. These net speeds agree with the observed apparent sound speed. This result suggests that the signals detected in time interval 1 could be the waves refracted multiple times in the troposphere.

D. Signals in time interval 2

In time interval 2, Fig. 3 indicates that the signals are detected at all sites. We choose the first and second maxima of the sound pressure detected at sites 1–6 in time interval 2. The travel time calculated for sites 5 and 6 reproduces the observed ones within an error of 10 s as shown in Table III. These signals detected at sites 5 and 6 are identified to be the rays turning from the stratosphere and the mesosphere as seen in Fig. 7. For site 4, the observed first signal is identified to be the ray turning from the stratosphere, whereas its travel time of the ray turning from the mesosphere is just outside time interval 2, and its end point is just outside site 4. The signals observed at sites 1–3 in time interval 2 have not been reproduced in the present calculations. One of the reasons why the calculations do not reproduce some of the observed signals is an underestimate in the stratospheric and mesospheric wind speeds in the wind models of HWM14 and MERRA-2 because of the space and time variation of

TABLE III. Comparison of the calculated and observed travel times of the signals detected at sites 1–6 in time intervals 2 and 3. In the third column, S indicates turning from the stratosphere, M from the mesosphere, and T from the thermosphere. The times τ_{cal} and τ_{obs} represent, respectively, the calculated and observed travel times of the signals from the source to the site.

	Time interval	Turning altitude	τ_{cal}	τ_{obs}	$\tau_{obs} - \tau_{cal}$
Site 1	TI 2			751	
				762	
	TI 3			777	
Site 2	TI 2			748	
				753	
	TI 3			795	
Site 3	TI 2			809	
				816	
				847	
Site 4	TI 2	S	975	974	-1
		M		996	
	TI 3	T	1228	1226	-2
			1240		
Site 5	TI 2	S	1000	1000	0
		M	1022	1021	-1
	TI 3	T	1243	1249	6
			1258	1268	10
Site 6	TI 2	S	1108	1118	10
		M	1121	1127	6
	TI 3	T	1309	1287	-22
			1352	1361	9

wind. See also Garcés *et al.* (2004) and Le Pichon *et al.* (2005).

E. Signals in time interval 3

In time interval 3, the observation shows that signals are detected at all sites as indicated by the red arrows in Fig. 3. The observed travel times of the signals at sites 1–3 are less than 40 s apart from the end of time interval 2, while those at sites 4–6 are more than 150 s apart from the end of time interval 2. According to the ray tracing, the signals detected at sites 4–6 are identified to be the rays turning from the thermosphere, and no ray turning from the thermosphere arrives at sites 1–3 as shown in Fig. 7. This result is consistent with the observation. However, the observations indicate that two signals arrived at the sites 5 and 6 and one signal was detected at site 4. The reason why only one signal was detected at site 4 is unclear at present. As for the observed signals close to time interval 2 at sites 1–3, the calculations predict that no ray arrives at sites 1–3.

V. SUMMARY AND DISCUSSION

On the basis of the dataset obtained by the densely distributed infrasound sensors on Shikoku Island in Japan, we have identified characteristic impulsive signals coming from the volcanic eruption at Mt. Shinmoedake on Kyushu Island on 10 March 2018 at all of the six observation sites, which are located between 200 km (site 1) and 340 km (site 6) away from Mt. Shinmoedake. We applied the ray tracing calculations to the analysis of the infrasonic waves in the frequency range between 0.05 and 0.3 Hz (wavelength range between 6 and 1 km) using the model atmosphere including the temperature profile provided by NRLMSISE-00 and the wind profiles provided by HWM14/MERRA-2.

We have shown that the observed signals can mostly be identified with one-to-one correspondence. The first waveform group having an observed propagation speed around 317 m/s is likely to be the waves propagated undergoing multiple refraction around an altitude of 10 km in the troposphere. On the other hand, the second waveform group detected at sites 4–6 is identified to be the waves turning from the stratosphere around 42 km and the mesosphere around 60 km. We have identified the third waveform group detected at the sites 4–6 to be the waves refracted from the lower thermosphere around 110 km. However, there are several signals that have not been reproduced by the ray tracing calculations such as the waveforms in the second and third groups detected at sites 1–3. One of the possibilities is that the stratospheric and mesospheric wind speeds were higher at the time of the event than those given by the wind model HWM14/MERRA-2 used in the present study. Another possibility is the limitation of the ray tracing method, which ignores wave behavior such as diffraction and scattering [see, e.g., Millet *et al.* (2007), Sabatini *et al.* (2019a), and Sabatini *et al.* (2019b)]. The present result demonstrates the importance of a dense and widely distributed infrasound observation network for the unambiguous

identification of various wave signals of the infrasound emitted by not only the volcano. Such observations are possibly useful also for the retrieval of subtle structures of wind and temperature, combined with ray tracing calculations and, if necessary, more detailed ones [e.g., Sabatini *et al.* (2019a) and Sabatini *et al.* (2019b)].

ACKNOWLEDGMENTS

We thank Dr. M. Ichihara for providing the data obtained by the microbarometer set by ERI near Mt. Shinmoedake and Dr. S. Watanabe and Dr. Y. Kakinami for fruitful discussion. The data provided by MERRA-2, HWM14, and NRLMSISE-00 are acknowledged. This work was partly supported by Ministry of Education, Culture, Sports, Science and Technology/Japan Society for the Promotion of Science (MEXT/JSPS) KAKENHI Grant No. 17H02062 and SECOM Science and Technology Foundation and ERI Joint Usage/Research Program (JURP) Grant Nos. 2014-B-15 and 2018-B-04.

- Bedard, A. J., and Georges, T. M. (2000). "Atmospheric infrasound," *Phys. Today* **53**(3), 32–37.
- Blom, P. (2019). "Modeling infrasonic propagation through a spherical atmospheric layer—Analysis of the stratospheric pair," *J. Acoust. Soc. Am.* **145**(4), 2198–2208.
- Campus, P. (2004). "The IMS infrasound network and its potential for detection of events: Examples of a variety of signals recorded around the world," *InfraMatics* **6**(1), 13–22.
- Christie, D. R., and Campus, P. (2010). "The IMS infrasound network: Design and establishment of infrasound stations," in *Infrasound Monitoring for Atmospheric Studies* (Springer Netherlands, Dordrecht), pp. 29–75.
- Drob, D. P., Emmert, J. T., Meriwether, J. W., Makela, J. J., Doornbos, E., Conde, M., Hernandez, G., Noto, J., Zawdie, K. A., McDonald, S. E., Huba, J. D., and Klenzing, J. H. (2015). "An update to the Horizontal Wind Model (HWM): The quiet time thermosphere," *Earth Space Sci.* **2**(7), 301–319.
- Garcés, M., Willis, M., Hetzer, C., Le Pichon, A., and Drob, D. (2004). "On using ocean swells for continuous infrasonic measurements of winds and temperature in the lower, middle, and upper atmosphere," *Geophys. Res. Lett.* **31**(19), L19304, <https://doi.org/10.1029/2004GL020696>.
- Gelaro, R., McCarty, W., Suárez, M. J., Todling, R., Molod, A., Takacs, L., Randles, C. A., Darmenov, A., Bosilovich, M. G., Reichle, R., Wargan, K., Coy, L., Cullather, R., Draper, C., Akella, S., Buchard, V., Conaty, A., da Silva, A. M., Gu, W., Kim, G.-K., Koster, R., Lucchesi, R., Merkova, D., Nielsen, J. E., Partyka, G., Pawson, S., Putman, W., Rienecker, M., Schubert, S. D., Sienkiewicz, M., and Zhao, B. (2017). "The Modern-Era Retrospective Analysis for Research and Applications, version 2 (MERRA-2)," *J. Clim.* **30**(14), 5419–5454.
- Global Modeling and Assimilation Office (GMAO) (2015). "MERRA-2 tavg3_3d_asm_Nv: 3d,3-Hourly,Time-Averaged,Model-Level,Assimilation, Assimilated Meteorological Fields V5.12.4."
- Headquarters for Earthquake Research Promotion (2013). "Evaluations of occurrence potentials or subduction-zone earthquakes (In Japanese)" https://www.jishin.go.jp/main/chousa/kaikou_pdf/nankai_2.pdf. (Last accessed May 15, 2020).
- Headlin, M. A. H., Garces, M., Bass, H., Hayward, C., Herrin, G., Olson, J., and Wilson, C. (2002). "Listening to the secret sounds of Earth's atmosphere," *Eos Trans. Am. Geophys. Union* **83**(48), 557–565.
- Ichihara, M. (2018). (private communication).
- Jones, R. M., and Bedard, A. J. (2018). "Atmospheric gravity wave ray tracing: Ordinary and extraordinary waves," *J. Atmos. Sol.-Terr. Phys.* **179**, 342–357.
- Landau, L., and Lifshitz, E. (1959). *Fluid Mechanics* (Elsevier Science, New York).
- Le Pichon, A., Blanc, E., Drob, D., Lambotte, S., Dessa, J. X., Lardy, M., Bani, P., and Vergnolle, S. (2005). "Infrasound monitoring of volcanoes to probe high-altitude winds," *J. Geophys. Res. Atmospheres* **110**(D13), D13106, <https://doi.org/10.1029/2004JD005587>.
- Lighthill, M. (1978). *Waves in Fluids* (Cambridge University Press, London).
- Millet, C., Robinet, J.-C., and Roblin, C. (2007). "On using computational aeroacoustics for long-range propagation of infrasounds in realistic atmospheres," *Geophys. Res. Lett.* **34**(14), L14814, <https://doi.org/10.1029/2007GL029449>.
- Picone, J. M., Hedin, A. E., Drob, D. P., and Aikin, A. C. (2002). "NRLMSISE-00 empirical model of the atmosphere: Statistical comparisons and scientific issues," *J. Geophysical Res. Space Phys.* **107**(A12), SIA15-1–SIA15-16, <https://doi.org/10.1029/2002JA009430>.
- Sabatini, R., Marsden, O., Bailly, C., and Gainville, O. (2019a). "Three-dimensional direct numerical simulation of infrasound propagation in the Earth's atmosphere," *J. Fluid Mech.* **859**, 754–789.
- Sabatini, R., Snively, J. B., Hickey, M. P., and Garrison, J. L. (2019b). "An analysis of the atmospheric propagation of underground-explosion-generated infrasonic waves based on the equations of fluid dynamics: Ground recordings," *J. Acoust. Soc. Am.* **146**(6), 4576–4591.
- Scott, J., Blanc-Benon, P., and Gainville, O. (2017). "Weakly nonlinear propagation of small-wavelength, impulsive acoustic waves in a general atmosphere," *Wave Motion* **72**, 41–61.
- Yamamoto, M.-y., and Yokota, A. (2015). "Infrasound monitoring for disaster prevention from geophysical destructions," *Proceedings of the 5th International Symposium on Frontier Technology 2015*, Kunming, China, pp. 24–28.